Showcasing research from Professor You's laboratory, Department of Chemical Engineering and Materials Science, Ewha Womans University, Seoul, Korea.

Chiral polymer hosts for circularly polarized electroluminescence devices

Electroluminescence devices producing circularly polarized luminescence (CPL) can substantially improve the brightness of three-dimensional (3D) displays for virtual reality. This research found that chiral polymer hosts are useful for boosting the performance of CPL electroluminescence devices. Polymer hosts tethering carbazole pendants in a helical half-eclipsed conformation exhibit strong intrinsic chiroptical behavior. The luminescence dissymmetry factor increases by an order of magnitude upon doping chiral phosphorescent Pt(II) complexes into the polymer hosts. The effect originates from diastereomeric interactions between the chiral host and dopant. The results demonstrate the effectiveness of diastereomeric control over CPL activities.

ROYAL SOCIETY OF **CHEMISTRY**

rsc.li/chemical-science

Chemical Science

EDGE ARTICLE

Chiral polymer hosts for circularly polarized electroluminescence devices†

Jayeon Hong,‡[a] Sangsub Kim,‡[b] Gyurim Park,[a] Yongmoon Lee,[b] Hyungchae Kim,[b] Sungjin Kim,[c] Tae-Woo Lee, [cd] Changsoon Kim [*b] and Youngmin You [*a]

Polymer electroluminescence devices producing circularly polarized luminescence (CP PLEDs) have valuable photonic applications. The fabrication of a CP PLED requires a polymer host that provides the appropriate chiral environment around the emitting dopant. However, chemical strategies for the design of chiral polymer hosts remain underdeveloped. We have developed new polymer hosts for CP PLED applications. These polymers were prepared through a free-radical polymerization of 3-vinylcarbazole with a chiral N-alkyl unit. This chiral unit forces the carbazole repeat units to form mutually helical half-sandwich conformers with preferred (P)-helical sense along the polymer main chain. Electronic circular dichroism measurements demonstrate the occurrence of chirality transfer from chiral monomers to achiral monomers during chain growth. The (P)-helical-sense-enriched polymer interacts diastereoselectively with an enantiomeric pair of new phosphorescent (R)- and (S)-dopants. The magnitude of the Kuhn dissymmetry factor (g_{abs}) for the (P)-helically-enriched polymer film doped with the (R)-dopant was found to be one order of magnitude higher than that of the film doped with the (S)-dopant. Photoluminescence dissymmetry factors (g_{PL}) of the order of 10^{-3} were recorded for the doped films, but the magnitude of diastereomeric enhancement decreased to that of g_{abs}. The chiral polymer host permits faster energy transfer to the phosphorescent dopants than the achiral polymer host. Our photophysical and morphological investigations indicate that the acceleration in the chiral polymer host is due to its longer Förster radius and improved compatibility with the dopants. Finally, multilayer CP PLEDs were fabricated and evaluated. Devices based on the chiral polymer host with the (R)- and (S)-dopants exhibit electroluminescence dissymmetry factors (g_{EL}) of 1.09×10^{-4} and -1.02×10^{-4} at a wavelength of 540 nm, respectively. Although challenges remain in the development of polymer hosts for CP PLEDs, our research demonstrates that chiroptical performances can be amplified by using chiral polymer hosts.

Introduction

Circularly polarized luminescence (CPL) refers to the differential emission between left- (LCPL) and right-handed circularly polarized light (RCPL). The two handedness of CPL has unique photonic utility: it makes possible the fabrication of 3D optical displays,[1,2] bioprobes,[3–5] biolabels,[6] spintronic devices,[7,8] security tags,[9] lasers,[10] enantioselective sensors,[11,12] quantum encryption,[13–15] and photocatalysts for asymmetric syntheses.[16] This utility is expected to be maximized by the development of CPL sources with high brightness and large dissymmetry factor values. Of the various classes of CPL sources,[17–33] polymer light-emitting devices producing inherent CPL (CP PLEDs) are particularly valuable. The relevant polymers are compatible with solution processes, which enables the fabrication of devices with large active areas at low cost. The majority of CP

[a]Division of Chemical Engineering and Materials Science and Graduate Program in System Health Science and Engineering, Ewha Womans University, Seoul 03760, Republic of Korea. E-mail: odds2@ewha.ac.kr

[b]Graduate School of Convergence Science and Technology and Inter-University Semiconductor Research Center, Seoul National University, Seoul 08826, Republic of Korea. E-mail: changsoon@snu.ac.kr

[c]Department of Materials Science and Engineering, Seoul National University, Seoul 08826, Republic of Korea

[d]School of Chemical and Biological Engineering, Research Institute of Advanced Materials, Institute of Engineering Research, Nano Systems Institute (NSI), Seoul National University, Seoul 08826, Republic of Korea

PLEDs developed to date contain CPL-active small molecular dopants that are doped into CPL-inactive polymers.[20,21,25,29,34–37] Intrinsically CPL-active polymers based on poly(fluorene),[22,38–46] poly(p-phenylenevinylene),[30,47] poly(p-phenyleneethylene),[48] poly(silane),[49,50] poly(thiophene),[51,52] and poly(dibenzofulvene)[53] have been developed.

Recent studies have found that the performances of CP PLEDs can be improved by providing an external asymmetric milieu around the emitting center. Di Nuzzo and co-workers obtained CP electroluminescence with a high electroluminescence dissymmetry factor ($|g_{EL}|$, $g_{EL} = 2(I_{LCPL} − I_{RCPL})/(I_{LCPL} + I_{RCPL})$ where I_{LCPL} and I_{RCPL} are electroluminescence intensities of LCPL and RCPL, respectively) of 0.8 from PLEDs employing poly(fluorene-alt-benzothiadiazole) with tethered chiral alkyl branches.[54] The high $|g_{EL}|$ value is attributed to the extrinsic polarization provided by chiral cholesteric phases formed upon thermal annealing of the polymer. Kim and co-workers obtained a very high $|g_{EL}|$ value of 1.13 from multilayer PLEDs.[34] In these devices, a rubbed poly(imide) layer and a non-emissive chiral dopant are present in order to convert linearly polarized luminescence into CPL. Despite these high $|g_{EL}|$ values, these strategies have several intrinsic drawbacks. The presence of insulating additives and multidomains can adversely influence charge carrier behavior. In addition, extrinsic modulation relies on the macroscopic formation of chiral phases and is likely to be sensitive on the film-forming conditions.

Inspired by the above studies, we decided to explore the idea that a chiral-at-main chain polymer host could be used to create an asymmetric milieu at the molecular level. In particular, we were intrigued by the idea that a chiral polymer could exert diastereoselective effects on the chiroptical activities of homochiral dopants (Fig. 1). The molecular structures of our polymer hosts are based on poly(3-vinylcarbazole). The carbazole unit has been widely employed in polymer hosts because of its favorable characteristics, including a large charge carrier mobility, and a wide bandgap and a high triplet-state energies.[55,56] Previous studies have investigated chiral polymers bearing carbazoles, but with a focus on their non-chiroptical properties.[57–67] CPL-emitting polymers with a carbazole emissive unit have recently been developed.[68,69] However, carbazole-based polymer hosts have not previously been utilized in CP PLEDs. Our polymer structure is intended to generate an intrinsic helical sense between adjacent carbazoles. Carbazole possesses a chiral (R)-α-phenylisopropyl moiety at its nitrogen atom. We expected that this chiral substituent would exert an asymmetric bias during polymerization, favoring one helical sense between the two adjacent carbazoles. A copolymer was also synthesized using achiral monomers to examine the chirality transfer during the course of its chain growth.

This strategy has particular potential because it requires neither chiral additives nor post-thermal treatments. Herein, we report our research into the development of chiral polymer hosts for use in CP PLEDs. The polymers were characterized by employing a variety of techniques, including structural, thermal, and spectroscopic methods. An enantiomeric pair of phosphorescent dopants based on cyclometalated Pt(II) complexes were newly created for our study. The diastereomeric interactions between the polymer hosts and the phosphorescent dopants were examined, with particular focus on chiral amplification and chirality-controlled energy transfer. Finally, CP PLEDs employing the chiral or achiral polymer hosts were fabricated, and their CP electroluminescence behaviors were compared. Our results demonstrate that chiroptical performances can be amplified by using chiral polymer hosts, while such an amplification is obscured within devices. This study undertook the first systematic research on chiral-at-main chain polymer hosts for CP PLEDs, which can provide insights that will be useful for the future development of CP PLEDs.

Results and discussion

Syntheses and structural characterizations of the polymer hosts

Our syntheses commenced with the tosylation of (R)-1-phenyl-2-propanol. The tosylate (1 in Scheme 1) was reacted with carbazole in the presence of potassium hydroxide and 18-crown-6. A Vilsmeier–Haack formylation reaction was then used to install a formyl unit on the carbazole adduct. Finally, Wittig-type olefination was performed on the aldehyde by using methyltriphenylphosphonium bromide and potassium carbonate to furnish the chiral monomer (4). The achiral monomer (5) was also prepared through olefination of the commercially available N-ethyl-3-carbazolecarboxaldehyde. The details of the syntheses are presented in the ESI section.† The chemical structures of the
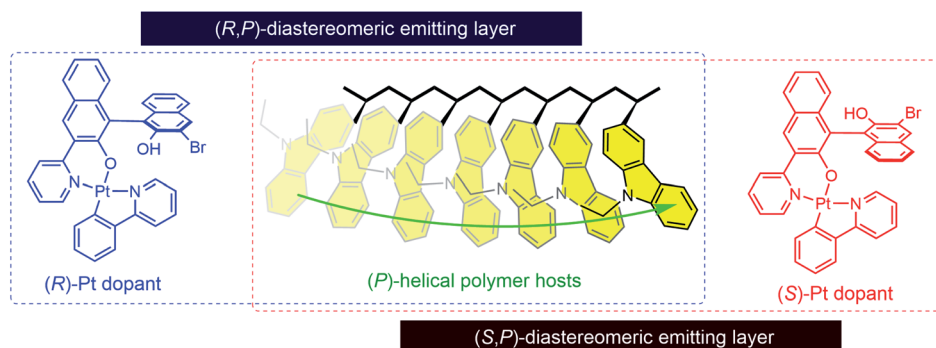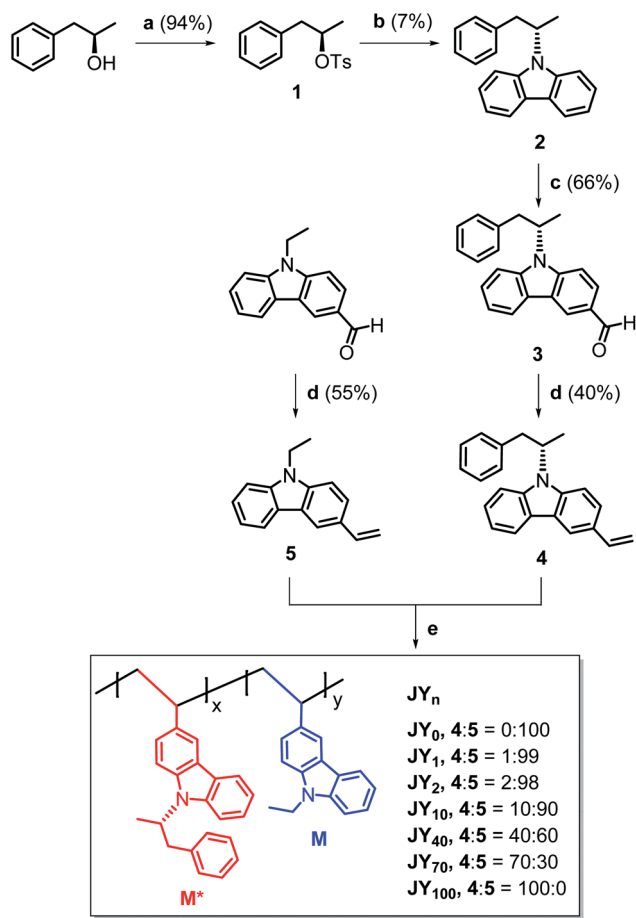

Fig. 1 Diastereomeric interactions between dopants and polymer hosts with enriched helical sense.

Scheme 1 Syntheses of the polymer hosts (JY_n). n is the mole percentage of the chiral monomer (M*) in the feed. Conditions: (a), TsCl, pyridine, Ar, rt, 1 day; (b), (i) carbazole, KOH, 18-crown-6, DMSO, 80 °C, 1 h, (ii) 1, 80 °C, 2 days; (c), (i) POCl₃, DMF, 0 °C, Ar, 1 h, (ii) 2, 110 °C, Ar, 1 day; (d), Ph₃PCH₃Br, K₂CO₃, 1,4-dioxane : H₂O = 12 : 1 (v/v), reflux, Ar, 4 days; (e), 4 : 5 = 1–0 : 1 (mol/mol), 2 mol% AIBN, degassed NMP, 65 °C, 2 days.

monomers and their precursors were characterized with standard spectroscopic techniques, including ¹H and ¹³C{¹H} NMR spectroscopy and high-resolution mass spectrometry. The

spectroscopic identification data were found to be fully consistent with the proposed structures (ESI).†

Conventional free-radical polymerization was performed with 4 and 5. A NMP solution containing the monomers and 2 mol% azobisisobutyronitrile (AIBN) initiator was thoroughly degassed with repeated vacuum–freeze–thaw cycles, and then heated at 65 °C for two days. The comonomer feed ratio of 4 : 5 was varied from 0 : 100 to 100 : 0. The resulting homopolymers (JY_0 and JY_{100}) and statistical copolymers (JY_1, JY_2, JY_{10}, JY_{40}, and JY_{70}) were purified through repeated precipitation in methanol. Here, the subscript n in JY_n refers to the mole percentage of 4 in its monomer feed. As summarized in Table 1, the conversion yields are in the range 68–80%. The conversion yield decreases with n, which is probably due to the steric hindrance exerted by the (R)-α-phenylisopropyl unit in 4. The number-averaged molecular weight (M_n) values of the copolymers were determined with GPC by using a Shodex® standard to be in the range 8700–13 000 Da. Their polydispersity index (PDI) values are in the range 1.8–2.5, which is typical of free-radical polymerizations. Although it is tempting to correlate n with M_n, the two parameters do not exhibit a clear proportionality. This absence of a proportionality and the inverse relationship between n and the conversion yield, suggest that chain growth between chiral monomers is disfavored.

¹H NMR spectroscopy (300 MHz, CD₂Cl₂) was employed to determine the ratio of the numbers of chiral (M*) and achiral (M) repeat units. As shown in Fig. 2a, the proton peaks belonging to M* and M are distinguishable. As expected, increasing the feed ratio of 4 yields a greater fraction of M* in the polymer chains. However, there is a concave deviation from linearity in the relationship between these two parameters (Fig. 2b); the fraction of M* in the polymer chain (i.e., [M*]/([M*] + [M])) is lower than the fraction of 4 in the monomer feed (i.e., [4]/([4] + [5])). This nonlinearity indicates that the reactivity with respect to polymerization of 4 is inferior to that of 5. The glass transition temperature (T_g, 10 °C min⁻¹) of JY_0 was determined to be 194 °C, and found to decrease in proportion with n (Fig. 2c and Table 1). This inverse relationship is probably due to the increase in free volume provided by the bulky (R)-α-phenylisopropyl unit in M*. In contrast, the degradation temperature, defined here as the temperature when the residual weight

Table 1 Structural and thermal parameters of the JY_n polymers

	Comonomer feed ratio ([4] : [5])	Yield[a] (%)	Repeat unit ratio[b] ([M*] : [M])	$T_g{}^c$ (°C)	$T_{d,90}{}^d$ (°C)	$M_n{}^e$	$M_w{}^f$	PDI[g]
JY_0	0 : 100	80	0 : 100	194	408	13 000	30 000	2.3
JY_1	1 : 99	79	2 : 98	190	411	10 000	18 000	1.8
JY_2	2 : 98	82	4 : 96	190	411	10 000	18 000	1.8
JY_{10}	10 : 90	71	7 : 93	170	401	7400	14 000	2.0
JY_{40}	40 : 60	72	30 : 70	164	398	8700	19 000	2.2
JY_{70}	70 : 30	73	53 : 47	150	401	8800	21 000	2.4
JY_{100}	100 : 0	68	100 : 0	140	399	12 000	30 000	2.5

[a] Conversion yields. [b] The chiral (M*) and achiral (M) repeat units molar ratio determined with ¹H NMR spectroscopy. [c] Glass transition temperature. [d] Temperature at which 10% decomposition occurs (heating rate = 10 °C min⁻¹). [e] Number average molecular weight. [f] Weight average molecular weight. The M_n and M_w values were determined with gel permeation chromatography (THF, Shodex® standard) techniques. [g] Polydispersity index, M_w/M_n.
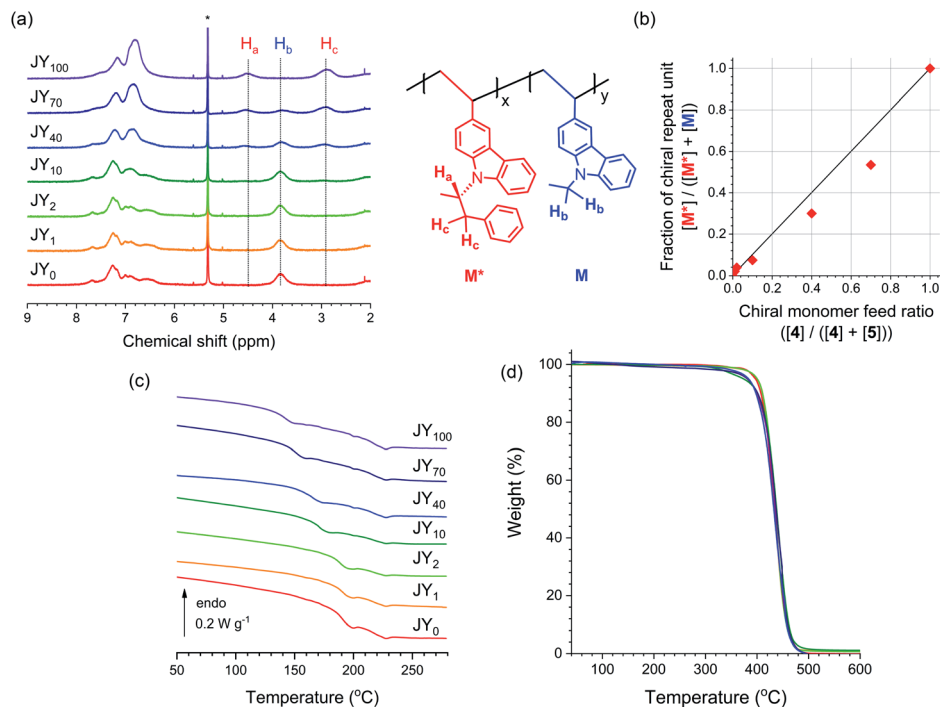
Fig. 2 (a) ^{1}H NMR (300 MHz, CD$_2$Cl$_2$) spectra of the JY$_n$ polymers (6 mg mL^{-1}). The peak marked with an asterisk is due to residual solvent. The structure on the right shows the assignments for H_a, H_b and H_c. The ratio of the integrated values of H_b and H_c corresponds to the ratio of the numbers of chiral (M*) and achiral (M) repeat units. (b) Fraction of chiral repeat units in the polymer (*i.e.*, [M*]/([M*] + [M])) as a function of the mole fraction of the chiral monomer in the feed (*i.e.*, [**4**]/([**4**] + [**5**])). (c) Differential scanning calorimetry results recorded during the first scan of the JY$_n$ polymers (heating rate = 10 °C min^{-1}). (d) Thermogravimetric analyses for the JY$_n$ polymers (heating rate = 10 °C min^{-1}). The structural and thermal parameters are summarized in Table 1.

reaches 90% ($T_{d,90}$), varies only very slightly with n. This result indicates that the presence of the chiral group in the copolymers has insignificant effects on their thermal stability (Fig. 2d and Table 1).

Chiroptical properties of polymer hosts

The host actions of the JY$_n$ polymers are likely to be sensitive to the helical sense. This claim is based on the fact that the mutual disposition of the carbazoles dictates the chiroptical properties of the polymers. An axial chirality (*i.e.*, helical sense) of carbazole pendants emerges when the main chain is isotactic with the carbazole pendants must be helically disposed due to steric interactions. This carbazolyl conformer can have in either a right-handed or a left-handed helical sense, which we define as (*P*)- and (*M*)-axial chirality, respectively. In contrast, axial chirality is not present when the main chain is syndiotactic. Fig. 3a displays the UV-vis absorption spectra of neat films of the JY$_n$ polymers spin-coated onto quartz substrates. The spectra contain three major bands with peak wavelengths at 352, 308, and 265 nm. Based on quantum chemical calculations for carbazole, Belletête *et al.* assigned the longest (*i.e.*, 352 nm) and medium (*i.e.*, 308 nm) wavelength absorption bands to the short- and long-axis electronic transitions, respectively (see the structures in the inset in Fig. 3a).[70] These bands also appear in the spectrum of a 10 μM model compound of M* (*i.e.*, **2** in Scheme 1), which indicates that they are among the intrinsic transitions of monomeric carbazole. The absence of any new

absorption bands excludes ground-state interactions in the JY$_n$ polymers.

In contrast to the UV-vis absorption spectra, the fluorescence spectra of **2** and the JY$_n$ polymers differ significantly (Fig. 3b). The fluorescence spectrum of a 10 μM solution of **2** (CH$_2$Cl$_2$) retains the characteristic vibronic progressions of carbazole with a peak wavelength of 350 nm. This spectral signature disappears in the fluorescence spectra of JY$_n$, and a broad emission band emerges with a bathochromically shifted peak wavelength at *ca.* 420 nm. The fluorescence spectra also contain shoulder bands in the region 380–384 nm. The peak and shoulder emissions can be assigned to originate from the excimers of a full-sandwich carbazole pair and a half-sandwich carbazole pair, respectively (see the structures in the inset in Fig. 3b), on the basis of the earlier study by Johnson.[71] The excimer assignments are supported by long rise profiles of the transient photoluminescence signals at 420 nm (ESI, Fig. S1†).[72–77] The full-sandwich excimers are observed for fully eclipsed conformers of carbazoles along the polymer chain, whereas the half-sandwich excimers are observed for staggered or half-eclipsed conformers. Note that the intensity of the shoulder band increases with n; this trend indicates that the bulky substituent in the chiral repeat unit preferentially disfavors the formation of the fully eclipsed conformers of full-sandwich excimer fluorescence.

The presence of half-sandwich excimers points to an axially chiral alignment of carbazoles along the polymer main chain.
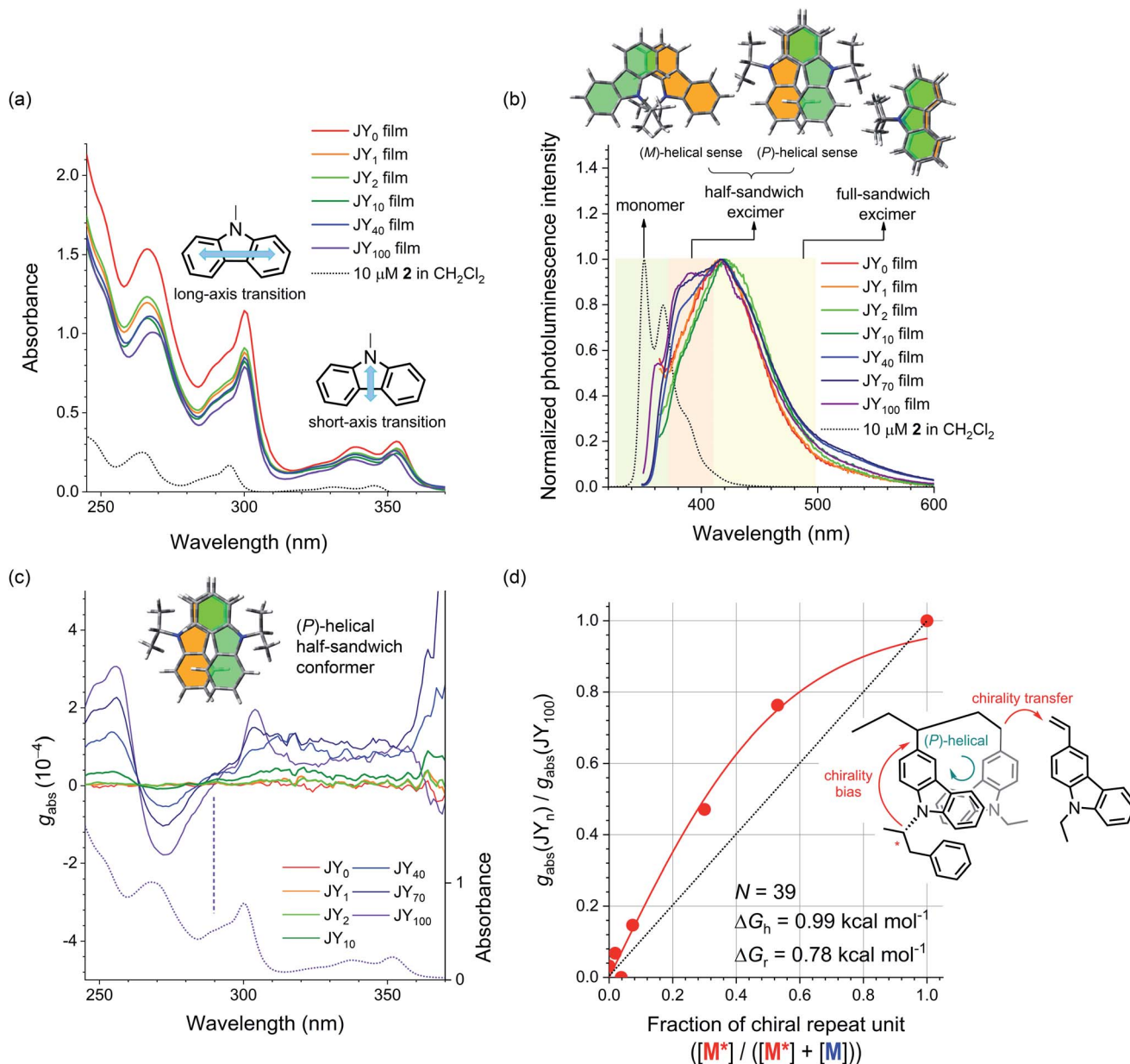
Fig. 3 (a) UV-vis absorption spectra of neat films of the JY_n polymers spin-coated onto quartz substrates. The black dotted curve is the UV-vis absorption spectrum of a 10 μM solution of **2** (CH_2Cl_2). The insets show the short- and long-axis transitions of carbazole. (b) Fluorescence spectra of neat films of the JY_n polymers ($\lambda_{ex} = 339$ nm). The black dotted curve is the fluorescence spectrum of a 10 μM solution of **2** (CH_2Cl_2). The colored regions highlight the monomeric emission of carbazole (green) and the carbazole excimer emissions of a half-sandwich conformer (beige) and a full-sandwich conformer (yellow). The structures at the top depict the two half-sandwich conformers and the full-sandwich conformer. (c) Plots of the Kuhn dissymmetry factor (g_{abs}) as a function of wavelength for neat films of the JY_n polymers cast onto quartz substrates. See ESI, Fig. S5† for the corresponding ECD spectra. The dotted curve is the UV-vis absorption spectrum of a neat film of the JY_{100} polymer. The positive Cotton effect in the long-axis transition reflects the (P)-helical sense of the half-sandwich conformer of carbazoles (see the inset). (d) A plot of the normalized g_{abs} values ($\lambda = 304$ nm) for the JY_n polymers (i.e., $g_{abs}(JY_n)/g_{abs}(JY_{100})$) as a function of the chiral repeat unit fraction in the polymers (i.e., $[M^*]/([M^*] + [M])$). The red curve is the nonlinear least-squares fit of the data to eqn (1). The inset shows the chirality transfer from the chiral monomer to the achiral monomer during the polymerization (see the inset).

To identify their helical sense, electronic circular dichroism (ECD) spectra of the JY_n polymer films were obtained. Fig. 3c displays the normalized ECD curves, which were constructed with the Kuhn dissymmetry factor (g_{abs}). g_{abs} is defined as $g_{abs} = 2(\varepsilon_{LCPL} - \varepsilon_{RCPL})/(\varepsilon_{LCPL} + \varepsilon_{RCPL})$, where ε_{LCPL} and ε_{RCPL} are the molar absorbance for the left- and right-handed circularly

polarized light, respectively.[78,79] Bisignate signals emerge for JY_n for $n > 2$. Negative and positive couplets are evident in the crossing points of the abscissa at 263 and 290 nm, respectively. The silence of the bisignate couplets for JY_{1-2} indicates insufficient induction of helical sense. Comparison of these spectra with the UV-vis absorption spectra reveals that the latter couplet

corresponds to the long-axis transition of carbazole. This observation indicates that there is asymmetric coupling between the long-axis-transition excitons of the vicinal carbazoles along the polymer main chain. This conclusion is supported by the absence of ECD signaling at 290 nm for a highly concentrated solution of the model compound of M* (i.e., 2; ESI, Fig. S2a†). Interchain asymmetric exciton coupling is also excluded because g_{abs} is virtually constant for JY_{100} solutions with various concentrations (0.017–0.17 mg mL^{-1} in 1,2-dichloroethane; ESI, Fig. S2b†).

The conformation of the carbazoles can be assigned to the (P)-helical sense, according to Nakanishi and Harada's exciton chirality rule.[80,81] The g_{abs} values of the couplets increase with n, with the largest $|g_{abs}|$ value of 3.1×10^{-4} found for JY_{100} at 255 nm. Note that this proportionality also parallels that of the relative fluorescence intensity of the half-sandwich excimer. This parallel suggests that both the ECD and the excimer fluorescence originate from the helical carbazole conformers. This notion is supported by a decrease in the ECD signals of JY_{100} (0.028 mg mL^{-1} in 1,2-dichloroethane) at elevated temperatures (ESI, Fig. S3†). The temperature dependence is fully reversible, which points to its conformational nature.

Finally, we determined whether chirality transfer occurs along the polymer main chain. To test this hypothesis, we plotted g_{abs} ($\lambda = 304$ nm) normalized to that of JY_{100} as a function of the fraction of M* (i.e., [M*]/([M*] + [M])). As shown in Fig. 3d, a convex deviation from linearity is found: the normalized g_{abs} is located above the linear relationship to the fraction of M*. This nonlinearity indicates the presence of chirality interactions between M* and the achiral monomer 5 during the polymerization. This chirality interaction is of an intrachain origin,[82,83] because N-ethylcarbazole films doped with 2 (0.5–15 wt%) do not show any ECD signaling (ESI, Fig. S4†). Such chirality interaction is expected to involve transfer of the point chirality in the carbazole pendant to the polymer main chain under the chiral random field exerted by (R)-α-phenylisopropyl, followed by propagation of the chirality along the main chain during the course of chain growth (see Fig. 3d). The first chirality transfer is governed by the chiral bias

energy (ΔG_h), and the second chirality transfer must overcome the chirality reversal energy (ΔG_r). Adopting Selinger's solutions to the Ising model,[84–86] we fitted the normalized g_{abs} curve to the following equation:

$$\frac{g_{abs}(JY_n)}{g_{abs}(JY_{100})} = \tanh\left[\frac{\Delta G_h}{RT} \times \frac{[M^*]}{[M^*] + [M]} \times \left(\frac{1}{\exp(\Delta G_r/RT)} + \frac{1}{N}\right)\right]$$

(1)

In eqn (1), R is the gas constant, T is 300 K, and N is the degree of polymerization. Note that N ranges from 39 for JY_{100} to 59 for JY_0, but its variation does not alter the fit results. Our nonlinear least-squares fit returned $\Delta G_h = 0.99$ kcal mol^{-1} and $\Delta G_r = 0.78$ kcal mol^{-1}. Although other combinations of ΔG_h and ΔG_r are possible, this ΔG_h value is similar to that of copolymers based on poly(isocyanate) with achiral and chiral alkyl branches, whereas ΔG_r is one order of magnitude smaller than that of poly(isocyanate).[87] The lower driving force for forming a chiral domain (i.e., small ΔG_r) in JY_n is expected considering that free-radical polymerization usually exhibits low stereoselectivity. Table 2 lists the photophysical and chiroptical parameters of JY_n.

## Diastereomeric interactions between the polymer hosts and the phosphorescent dopant

To assess the utility of our polymer hosts, we synthesized an enantiomeric pair of phosphorescent Pt(II) complex dopants, (R)- and (S)-Pt (Scheme 2). The molecular structure of the dopants is based on a square planar complex of Pt(II), where the ligands with C^N and N^O motifs are coordinated with Pt. The N^O ligand contains axially chiral 1,1′-bi-2-naphthol, which endows the complexes with chiroptical properties. (R)- and (S)-Pt were prepared with a two-step synthesis. A Pd(0)-catalyzed Stille reaction between homochiral 3,3′-dibromo-1,1′-bi-2-naphthol and 2-(tributylstannyl)pyridine furnished a monopyridinylated product. The reaction did not proceed further to a bipyridinylated product, even in the presence of excess amounts of the catalyst and 2-(tributylstannyl)pyridine. Finally, the monopyridinylated ligand was reacted with a μ-dichloro

Table 2 Photophysical and chiroptical properties of the JY_n polymers[a]

	λ_{abs}[b] (nm)	λ_{em}[c] (nm)	g_{abs} (10^{-4}, λ_{obs}[d] = 304 nm)	τ_{obs}[e] (ns)	PLQY[f]	k_r[g] (10^7 s^{-1})	k_{nr}[h] (10^7 s^{-1})
JY_0	308, 353	418	0.063	15	0.18 (±0.046)	1.2	5.5
JY_1	308, 353	418	0.13	15	0.12 (±0.004)	0.73	5.9
JY_2	308, 353	420	0.056	15	0.16 (±0.027)	1.1	5.6
JY_{10}	308, 353	420	0.29	9.1	0.23 (±0.029)	2.5	8.5
JY_{40}	308, 353	384 (sh), 417	0.92	12	0.20 (±0.025)	1.7	6.7
JY_{70}	308, 352	382 (sh), 417	1.5	10	0.26 (±0.015)	2.6	7.4
JY_{100}	308, 352	380 (sh), 417	2.0	15	0.26 (±0.008)	1.7	4.9

[a] Neat films of JY_n spin-cast onto quartz substrates. [b] Absorption peak wavelengths. [c] Emission peak wavelengths. λ_{ex} = 339 nm. sh = shoulder. [d] Kuhn dissymmetry factor determined at a wavelength of 304 nm. [e] Photoluminescence lifetimes determined at λ_{em} by using the time-correlated single-photon-counting techniques after picosecond pulsed laser excitation at 377 nm (temporal resolution = 0.025 ns). [f] Absolute PLQY values determined with an integrating sphere. These determinations were performed in triplicate with fresh samples. [g] The radiative decay rate (k_r) was calculated with the equation k_r = PLQY/τ_{obs}. [h] The non-radiative decay rate (k_{nr}) was calculated with the expression (1 − PLQY)/τ_{obs}.
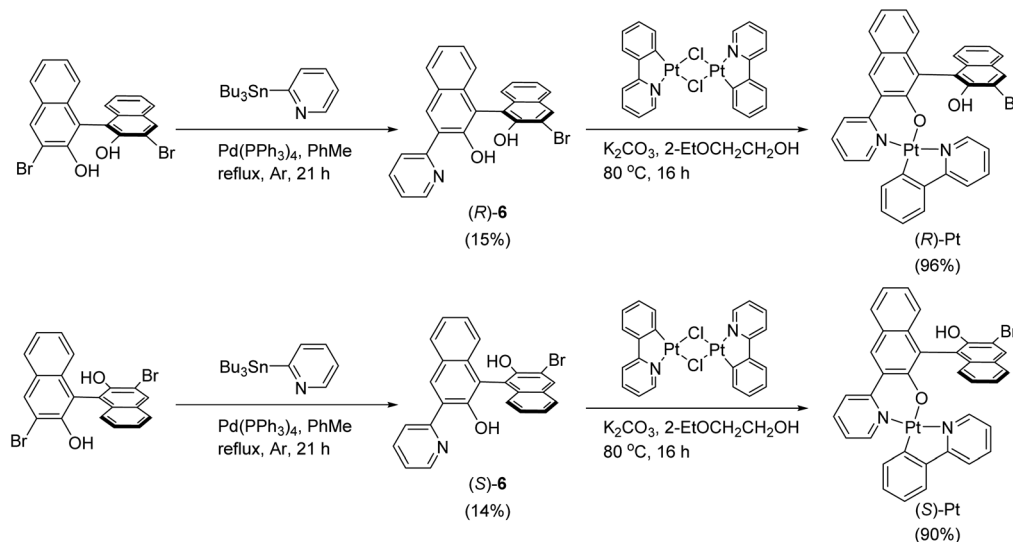
Scheme 2 Syntheses of the phosphorescent chiral dopants, (R)- and (S)–Pt.

dinuclear Pt(II) precursor in the presence of potassium carbonate to form (R)- or (S)-Pt. The presence of residual bromo and hydroxy groups in the Pt(II) complexes is deleterious to the performance of devices. The synthetic details and spectroscopic identification data are summarized in ESI.† The photophysical parameters of the Pt dopants are listed in Table 3.

We now investigated the intermolecular chirality interactions in the binary mixtures of these enantiomeric dopants and chiral polymer hosts. The maximum chiroptical properties are found for JY_{100}. We thus chose JY_{100} and its achiral control polymer, JY_0, for the rest of our studies. We aimed to determine whether the chiroptical behaviors of the Pt(II) dopants are influenced by the local chiral environments provided by the JY_{100} host. As shown in Fig. 4, the UV-vis absorption spectra of the neat films of JY_0 and JY_{100} are barely affected by the presence of 10 wt% (R)- or (S)-Pt, indicating there is little or no formation of ground-state species between the host and dopant. As expected, the ECD signals of the JY_0 films doped with (R)- and (S)-Pt (i.e., (R)-Pt:JY$_0$ and (S)-Pt:JY$_0$, respectively) are mirror images (Fig. 4a). Two major bands with peaks at 316 nm ($|g_{abs}| = 1.37 \times 10^{-4}$) and 372 nm ($|g_{abs}| = 2.2 \times 10^{-4}$) are evident. The former and the latter overlap with the ligand-centered (LC) transition bands and the metal-to-ligand charge-transfer (MLCT)

transition bands of the Pt(II) dopants, respectively. The magnitudes of g_{abs} of the MLCT transition bands are not sensitive to the configuration of the Pt dopants, which implies that the observed chiroptical properties are inherent to the dopants.

The ECD signals of the Pt:JY$_{100}$ films are dominated by those of JY$_{100}$, but the contributions from LC and MLCT regions of the Pt dopants are evident. As shown in Fig. 4b, the g_{abs} profiles of (R)- and (S)-Pt in JY$_{100}$ deviate from the mirror-image relationship found for JY$_{100}$. Subtracting the g_{abs} curve of the JY$_{100}$ neat film from those of the doped films (i.e., Δg_{abs}) provides more decisive evidence for dissymmetric ECD signals (see the bottom panel in Fig. 4b). The Δg_{abs} value of (R)-Pt:JY$_{100}$ is 5.7×10^{-4} at 391 nm which is greater than that of (R)-Pt:JY$_0$ (2.5×10^{-4}). On the contrary, an opposite behavior is found for (S)-Pt: the Δg_{abs} value of (S)-Pt:JY$_{100}$ is 0.50×10^{-4} at 391 nm which is smaller than that for (S)-Pt:JY$_0$ (1.7×10^{-4}). This stereoselectivity points to the presence of diastereoselective interactions between the chiral polymer host and the Pt dopants. Chiral repeat units are probably responsible for the diastereomeric effects, because g_{abs} of the MLCT transition band increases with the fraction of chiral repeat units (i.e., M*) in JY$_n$ (ESI, Fig. S6†).

The CPL behaviors of the Pt-doped JY films were characterized by using our home-made instrument based on

Table 3 Photophysical and chiroptical properties of the dopants[a]

	λ_{abs}[b] (nm)	λ_{em}[c] (nm)	g_{abs}[d] (10^{-3}, λ_{obs} = 372 nm)	τ_{obs}[e] (µs)	PLQY[f]	k_r[g] (10^4 s^{-1})	k_{nr}[h] (10^5 s^{-1})
(R)-Pt	262, 320, 400	590	−2.1	21	0.25	1.2	3.6
(S)-Pt	262, 320, 400	590	2.3	21	0.24	1.1	3.6

[a] 10 µM in Ar-saturated 1,2-dichloroethane. [b] Absorption peak wavelengths. [c] Emission peak wavelengths. λ_{ex} = 400 nm. [d] Kuhn dissymmetry factor determined at a wavelength of 372 nm. See ESI, Fig. S7 for the spectra. [e] Photoluminescence lifetimes of 100 µM Pt in Ar-saturated 1,2-dichloroethane determined with nonlinear least-squares fits of photoluminescence traces recorded at a wavelength of 590 nm employing time-correlated single-photon-counting techniques after picosecond pulsed laser excitation at 377 nm (temporal resolution = 10 ns). [f] Photoluminescence quantum yield determined relative to the 9,10-diphenylanthracene standard (PLQY = 1.00, toluene).[88] [g] The radiative decay rate (k_r) was calculated with the equation $k_r = PLQY/\tau_{obs}$. [h] The non-radiative decay rate (k_{nr}) was calculated with the expression $(1 − PLQY)/\tau_{obs}$.

Fig. 4 (a) UV-vis absorption (top), g_{abs} (middle), and the g_{abs} difference spectra (bottom; Δg_{abs}, $g_{abs}(10\ \text{wt\% Pt:JY}_0) - g_{abs}(\text{JY}_0)$) for the JY_0 films (quartz substrates) in the absence and presence of 10 wt% (R)-Pt or 10 wt% (S)-Pt. (b) UV-vis absorption (top), g_{abs} (middle), and the g_{abs} difference spectra (bottom; Δg_{abs}, $g_{abs}(10\ \text{wt\% Pt:JY}_{100}) - g_{abs}(\text{JY}_{100})$) for the JY_{100} films (quartz substrates) in the absence and presence of 10 wt% (R)-Pt or 10 wt% (S)-Pt.

Fig. 5 Circularly polarized luminescence of JY films doped with 30 wt% Pt dopants. Top, Photoluminescence spectra; middle, circularly polarized luminescence spectra; bottom, the variations in g_{PL} with wavelength.

a photoelastic modulator and a lock-in amplifier (see ESI†). Fig. 5 compares the photoluminescence and CPL spectra of JY_0 and JY_{100} doped with 30 wt% (R)- or (S)-Pt. The films produce broad emissions due to the MLCT transition of the Pt dopants; the spectra arising from the solutions are identical (ESI, Fig. S7†). The presence of CPL in the same wavelength range of the photoluminescence spectra indicates that the Pt dopants are responsible for its emergence. The signs of the photoluminescence dissymmetry factor (g_{PL}, $g_{PL} = 2(PI_{LCPL} - PI_{RCPL})/(PI_{LCPL} + PI_{RCPL})$ where PI_{LCPL} and PI_{RCPL} are photoluminescence intensities of LCPL and RCPL, respectively) for the (R)-Pt:JY_0 and (S)-Pt:JY_0 films are opposite, and are identical to those of the MLCT transition bands in the ECD spectra (Fig. 4). These results indicate that common electronic states with different spin configurations (i.e., singlet and triplet MLCT transition state) are involved in the absorption and photoluminescence transitions. A CPL spectrum obtained for a 100 mM solution of (R)-Pt is virtually identical to that of the (R)-Pt:JY_0 film (ESI, Fig. S8†). The maximum g_{PL} values of the (R)-Pt:JY_{100} and (S)-Pt:JY_{100} films are 1.0×10^{-3} ($\lambda_{em} = 540$ nm) and -0.94×10^{-3} ($\lambda_{em} = 545$ nm), respectively, which are slightly larger than the values of the corresponding films with the JY_0 host ((R)-Pt:JY_0, 0.65×10^{-3}; (S)-Pt:JY_0, -0.73×10^{-3}). There is possibly a diastereoselective effect in the g_{PL} spectra (see the bottom panel of Fig. 5). The differences between the $|g_{PL}|$ values of the (R)-Pt:JY films (i.e., the blue solid and empty circles) are greater than the differences between those of (S)-Pt:JY films (i.e., the red solid

and empty circles) around 550 nm, but the magnitudes of the differences are low.

One of key requirements for the host is the ability to trap excitons within a dopant. The formation of dopant excitons occurs through two pathways: one is Langevin recombination on a host, followed by exciton (energy) transfer to a dopant; the other is Shockley–Read–Hall recombination on a dopant. The exergonic energy transfer from the JY hosts to Pt dopants was directly monitored by using steady-state and transient photoluminescence techniques. A neat film of JY_0 was found to exhibit excimer emission of carbazoles at 428 nm upon photoexcitation at 339 nm. The host emission decreases in intensity with increases in the concentration of (R)-Pt (0–10 wt%), with the emergence of sensitized dopant emission at a peak wavelength of 586 nm (Fig. 6a). This decrease-and-increase profile indicates the presence of an active energy donor/energy acceptor pair. The titration isotherms of I_0/I, where I_0 and I are the host emission intensities ($\lambda_{em} = 420$ nm) in the absence

and presence of the dopant, respectively, follow rise profiles due to energy transfer (Fig. 6c). Qualitatively similar, but faster rises are observed for JY_{100} films doped with various concentrations of (R)-Pt (0–10 wt%). This result indicates that the energy transfer from JY_{100} to the Pt dopants occurs more rapidly than that from JY_0. The results for JY_n films with (S)-Pt are shown in ESI, Fig. S9.†

The faster energy transfer in the case of JY_{100} was also demonstrated by using transient photoluminescence experiments. The decay traces of the host emission were monitored at a wavelength of 420 nm after picosecond pulsed laser excitation at 377 nm. As shown in Fig. 6d and e, the transient emission signals decay following a biexponential decay model, which is probably due to film inhomogeneity (*vide infra*). The average photoluminescence lifetime (τ) of a neat film of JY_0 is 10 ns, which is typical of excimer fluorescence. τ decreases with increasing the concentration of the Pt dopant due to energy transfer. The apparent energy transfer rate (k_{ET}), which was
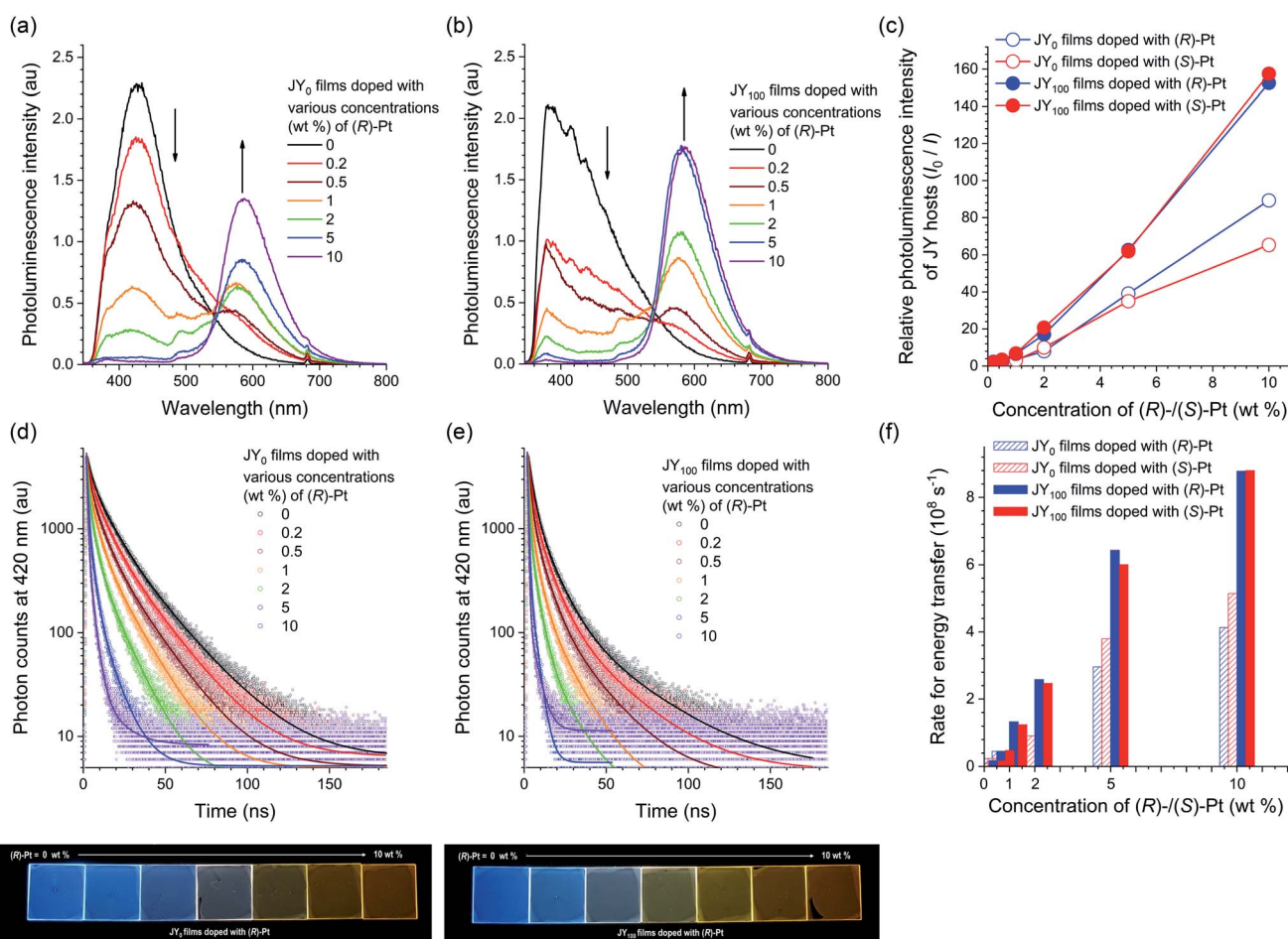

Fig. 6 (a and b) Photoluminescence spectra ($\lambda_{ex} = 339$ nm) for JY_0 (a) and JY_{100} (b) films doped with various concentrations (0–10 wt%) of (R)-Pt. The spectra of the films doped with (S)-Pt are shown in ESI, Fig. S9.† (c) Ratios of the photoluminescence intensities of the JY_n hosts in the absence over the presence of increased concentrations of the Pt dopants (I_0/I). (d and e) Photoluminescence decay traces ($\lambda_{obs} = 420$ nm) of JY_0 (d) and JY_{100} (e) films doped with various concentrations (0–10 wt%) of (R)-Pt obtained after picosecond pulsed laser photoexcitation at 377 nm (temporal resolution = 25 ps). The solid curves are nonlinear least-squares fits to a biexponential decay model. The decay traces of the films doped with (S)-Pt are shown in ESI, Fig. S9.† The decay traces of dopant emissions recorded at a wavelength of 590 nm are shown in ESI, Fig. S10.† The bottom photographs show the photoluminescence emissions of JY_0 (left) and JY_{100} (right) films doped with various concentrations of (R)-Pt visualized under photoirradiation at a wavelength of 365 nm. (f) Rates of energy transfer (k_{ET}) from the JY hosts to the Pt dopants.

calculated with the relationship $k_{ET} = 1/\tau - 1/\tau_0$ where τ and τ_0 are photoluminescence lifetimes in the presence and absence of the dopant, respectively, increases with the dopant concentration. It was found that k_{ET} is greater for JY_{100} in the tested concentration range (i.e., 0.2–10 wt%). A possible explanation for these different energy transfer behaviors could invoke the photophysical and structural properties of the JY hosts. Actually, the Förster radii of the JY_0 and JY_{100} films calculated based on a refractive index of 1.047 and the spectral overlap integrals with the Pt dopants are 25 and 27 Å, respectively. The longer Förster radius of JY_{100} is probably due to its greater PLQY (Table 2), and is consistent with its faster energy transfer behavior.

In addition, our microscopic experiments suggest that the phase homogeneity of JY_{100} might also contribute to its superior energy transfer behavior. Fig. 7 compares confocal laser-scanning fluorescence micrographs of JY_0 and JY_{100} films doped with identical concentrations (10, 30, and 50 wt%) of (S)-Pt. The bright puncta correspond to aggregates of (S)-Pt. It can be seen that the JY_0 films contain more dopant aggregates than the JY_{100} films. The poor phase homogeneity in JY_0 is also evident in the transmission electron micrographs (note the black dots in the inset images in Fig. 7c and d). The energy dispersive X-ray spectra confirm that there is Pt enrichment in the aggregates. In contrast, phase separation is effectively suppressed in the JY_{100} films. The different phase homogeneity is likely due to the differed free volumes of polymers. The bulky (R)-α-phenylisopropyl moiety retards the packing of polymer chains in JY_{100}, providing more rooms for the dissolution of the Pt dopants. The better phase homogeneity of JY_{100} permits the molecular level dispersion of the dopants within the Förster radius of the host. These results indicate that the faster energy

transfer of JY_{100} originates from both a longer Förster radius and improved compatibility with the Pt dopants. Finally, the energy transfer rates to (R)- and (S)-Pt are the same in JY_{100}. The lack of chirality-discriminated energy transfer is expected, as $|g_{PL}|$ values of the hosts ($<10^{-3}$) and of the $|g_{abs}|$ values of the dopants ($\sim10^{-4}$) are very small.

The Shockley–Read–Hall recombination has the following electrochemical requirements: (i) the oxidation potential (E_{ox}) of the host > E_{ox} of the dopant, and (ii) the reduction potential (E_{red}) of the host < E_{red} of the dopant. The redox potentials for the JY_n hosts and the Pt dopants were determined with cyclic voltammetry (CV) and differential pulse voltammetry (DPV). Fig. 8 displays the voltammograms of Ar-saturated THF containing JY_0, JY_{100}, and (R)- and (S)-Pt. JY_0 and JY_{100} exhibit irreversible oxidation at 1.25 and 1.22 V vs. standard calomel electrode (SCE), respectively. These peaks are close to E_{ox} of poly(N-vinylcarbazole) (1.39 V vs. SCE; ESI, Fig. S11†), which indicates that carbazole is responsible for the oxidation. The E_{ox} value of (R)- and (S)-Pt is 0.88 V vs. SCE, which is more cathodic than the E_{ox} values of the JY hosts. Therefore, hole trapping within the Pt dopants is thermodynamically favored with positive driving forces of 0.37 and 0.34 eV for JY_0 and JY_{100}, respectively. The E_{red} values calculated by subtracting the optical bandgap energies (3.43 eV for the JY hosts and 2.48 eV for the Pt dopants) from the E_{ox} values are −2.18 V (JY_0), −2.21 V (JY_{100}), and −1.60 V ((R)- and (S)-Pt) vs. SCE. The E_{red} value of the Pt complexes is more anodic than those of the JY hosts, which suggests that electron trapping by the dopants will be effective with thermodynamic driving forces of 0.58 eV (JY_0) and 0.61 eV (JY_{100}). These electrochemical results indicate that the JY_n
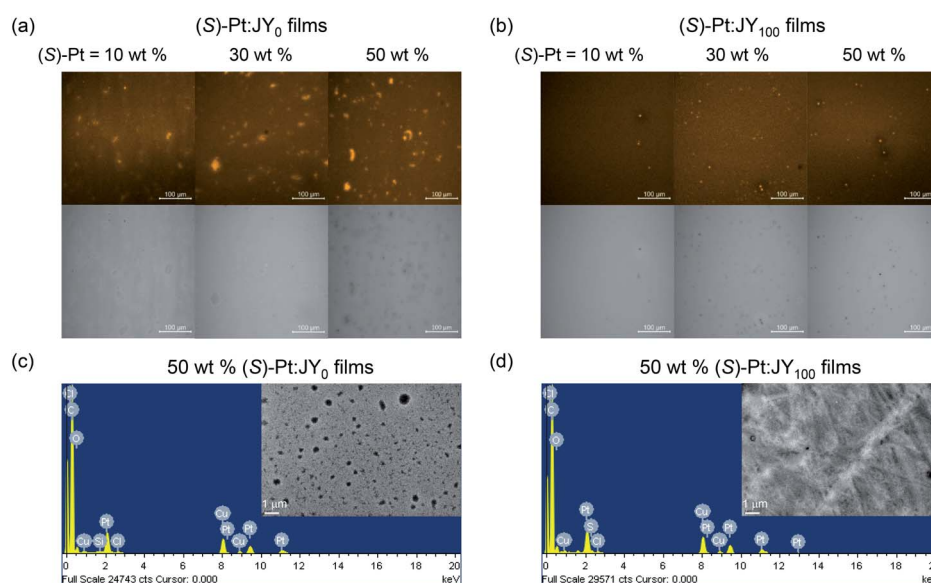

Fig. 7 (a and b) Confocal laser-scanning fluorescence micrographs ($\lambda_{ex} = 405$ nm, $\lambda_{obs} = 500–700$ nm) for JY_0 (a) and JY_{100} (b) films (quartz substrates) doped with various concentrations (10, 30 and 50 wt%) of (S)-Pt: top panels, fluorescence images; bottom panels, bright-field images. Scale bar = 100 μm. (c and d) Energy dispersive X-ray spectra and the average atomic percentage compositions of JY_0 (c) and JY_{100} (d) films doped with 50 wt% (S)-Pt (200 mesh carbon films on copper). The atomic percentage compositions of Pt were quantified for Cliff Lorimer thin ratio sections: 1.4% Pt for (S)-Pt:JY_0 films; 1.5% Pt for (S)-Pt:JY_{100} films. The insets show TEM images of the JY films doped with 50 wt% (S)-Pt. Scale bar = 1 μm.
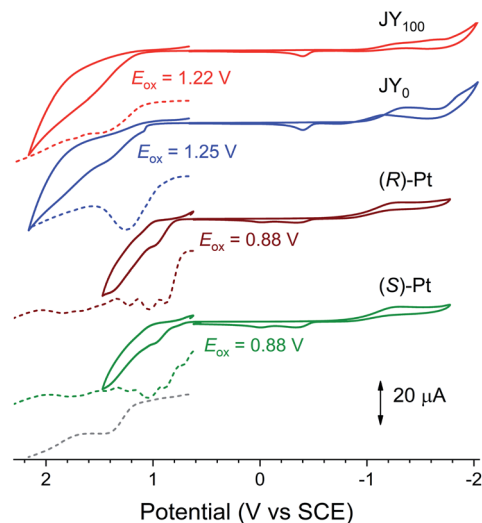
Fig. 8 Cyclic (solid curves) and differential pulse (dotted lines) voltammograms of Ar-saturated THF solutions of JY_{100} (red, 0.63 mg mL^{-1}), JY_0 (blue, 0.43 mg mL^{-1}), and (R)- (brown) and (S)-Pt (green, 2 mM). 0.10 M Bu$_4$NPF$_6$ was used as the supporting electrolyte. A Pt disk and a Pt wire served as the working and counter electrodes, respectively. A Ag/AgNO$_3$ pseudo reference electrode was used. Scan rates: 0.1 V s^{-1} (CV) and 0.004 V s^{-1} (DPV). The grey dotted line corresponds to blank signals (*i.e.*, Ar-saturated THF containing 0.10 M Bu$_4$NPF$_6$).

polymers will effectively confine charge carriers within the Pt dopants.

Circularly polarized electroluminescence

In the final stage of our study, we fabricated PLEDs with the following emitting layers (EMLs): (R)-Pt:JY_0, (S)-Pt:JY_0, (R)-Pt:JY_{100}, and (S)-Pt:JY_{100}. Fig. 9a depicts the energy-level diagram of our PLEDs with the configuration glass/ITO/50 nm GraHIL/50 nm EML/50 nm TPBi/1 nm LiF/100 nm Al (TPBi, 1,3,5-tris(N-phenylbenzimidazole-2-yl)benzene). To facilitate hole injection into the polymer hosts with deep levels of HOMO (the highest occupied molecular orbital, 6.0 eV), a conducting polymer hole injection layer denoted GraHIL, which is composed of poly(3,4-ethylenedioxythiophene):poly(styrenesulfonate) (PEDOT:PSS) and tetrafluoroethylene-perfluoro-3,6-dioxa-4-methyl-7-octenesulphonic acid, was used.[89] The dopant concentration in the EMLs was chosen to be 30 wt% to maximize the dopant emission (ESI, Fig. S12†). Fig. 9c and d show the current density–voltage–luminance (J–V–L) and external quantum efficiency (EQE)–J characteristics of the PLEDs, respectively. The values of V at $J = 5$ mA cm^{-2} range from 11.4 to 12.0 V, which suggests that, even with the use of GraHIL, hole injection into JY_0 and JY_{100} is somewhat inefficient. Nevertheless, all devices exhibit normal electroluminescence operation reliable for device characterization: the
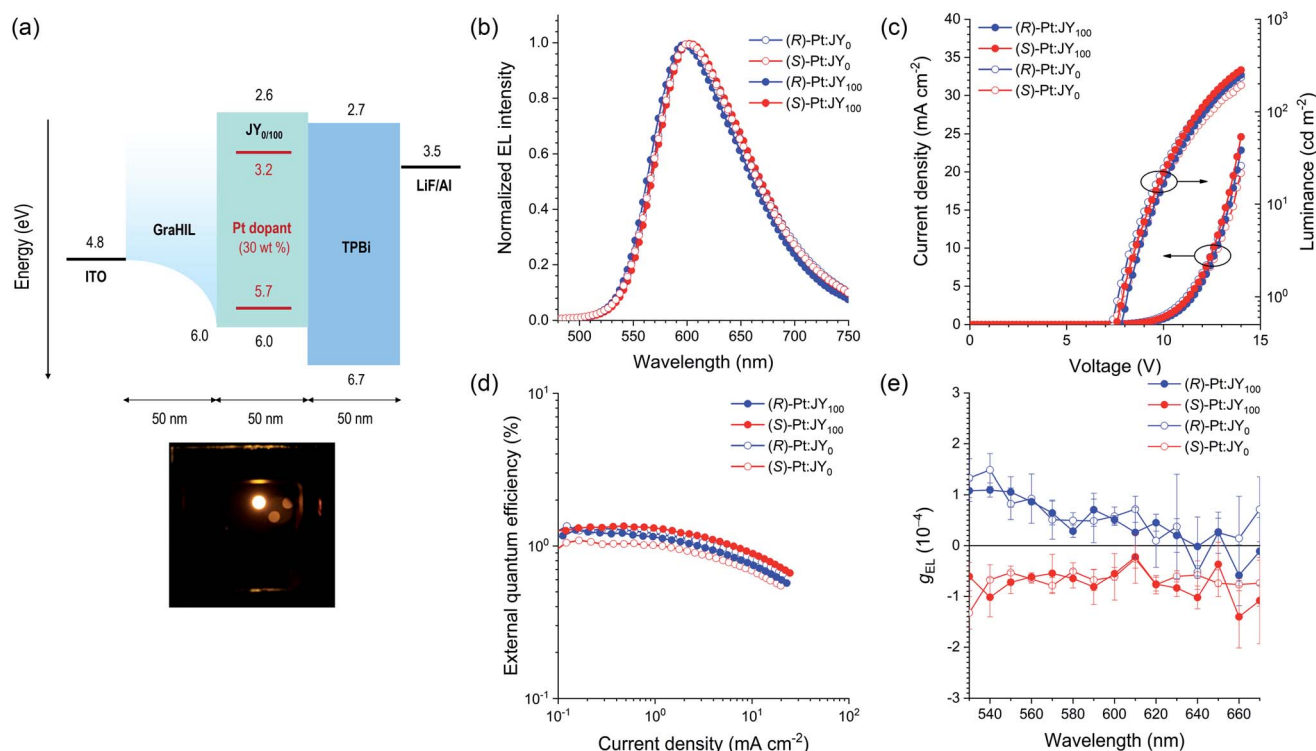

Fig. 9 (a) Energy-level diagram and device structure for the PLEDs with (R)- or (S)-Pt:JY_n emitting layers. The positions of the energy levels of the polymer hosts and the Pt dopants were determined with cyclic and differential pulse voltammetry, and the positions of the other levels have previously been reported.[89–91] The bottom photo shows the electroluminescence of the device. (b) Electroluminescence spectra recorded at a current density of 1.6 mA cm^{-2}. (c) Current density–voltage–luminance and (d) external quantum efficiency–current density characteristics of the PLEDs. (e) Spectra of g_{EL} recorded at a current density of 2.2 mA cm^{-2} averaged over 20 measurements. The error bars represent standard deviations.

electroluminescence spectra recorded at $J = 1.6$ mA cm^{-2} consist of dopant emission only (Fig. 9b), and are almost identical to one another and the photoluminescence spectra of the corresponding films (Fig. 5). The EQE–J curves are typical of phosphorescent PLEDs, although the peak EQE values are much smaller than those of state-of-the-art devices (Fig. 9d).

g_{EL} was measured as functions of the emission wavelength (Fig. 9e). For each device, the sign of g_{EL} is the same as that of g_{PL} over the entire range of emission wavelengths. The magnitude of g_{EL}, however, is smaller than that of g_{PL} by a factor of ca. 10. This difference is probably due to the presence of the metal electrodes in the PLEDs; CPL emitted toward the metal electrode reverses its handedness upon reflection at the metal surface,[21] and thus interferes with the CPL emitted toward the glass substrate with the opposite handedness. This hypothesis is consistent with our results for the EMLs deposited on quartz substrates, which shows that the signs of g_{PL} measured on the film and substrate sides are the same (ESI, Fig. S13†). Although the (R)-Pt:JY$_{100}$ film has lager g_{PL} values than the (R)-Pt:JY$_0$ film in the spectral region $\lambda_{em} < 590$ nm, this enhancement is not observed for g_{EL}; the g_{EL} values of the PLEDs with (R)-Pt:JY$_{100}$ and (R)-Pt:JY$_0$ EMLs are similar. The lack of enhancement in g_{EL} is possibly due to the multilayer structure of the PLEDs; the presence of the metal electrode, in particular, provides an optical environment that is different from that of the samples used in the photoluminescence studies (i.e., the EMLs on quartz substrates). It is anticipated that careful optical modeling of the PLEDs will enable diastereoselective enhancement in the CP electroluminescence.

Conclusions

We have developed and evaluated chiral polymer hosts for use in CP PLEDs. The polymers were synthesized through free radical polymerization of 3-vinylcarbazole. The vinyl monomer was modified to contain either the chiral (R)-α-phenylisopropyl moiety or the achiral ethyl group. The homopolymers and copolymers of the chiral and achiral monomers were structurally, thermally, and spectroscopically analyzed. Our analyses demonstrate that transfer of chirality from the chiral moiety in the monomer to the polymer main chain occurs during chain growth. In particular, the carbazole pendants form half-sandwich conformers with a mutually (P)-helical sense. This helical sense is not affected by variations in temperature or the concentrations of the polymer solutions, which indicates that the helical half-sandwich conformers are of intrachain origin. To evaluate the performances of the hosts, a novel enantiomeric pair of phosphorescent dopants was synthesized. We found g_{abs} increased for the diastereomeric mixture of the (R)-dopant and the (P)-helical polymer, whereas g_{abs} decreased for the diastereomeric mixture of the (S)-dopant and the (P)-helical polymer. Similar enhancements in g_{PL} are also observed. The chiral polymer host exhibits faster energy transfer to the dopants than the achiral polymer host, due to its longer Förster radius and better compatibility with the dopants. However, the energy transfer from the polymer host does not depend on the chirality of materials. This result indicates that the contribution of the chirality-controlled excited-state interactions between the host and dopant is negligible. The PLED based on the (P)-helical polymer and the (R)-dopant was found to exhibit a g_{EL} value of 1.09×10^{-4} ($\lambda_{em} = 540$ nm) and an EQE of 1.2%. This study has demonstrated that selection of the chiral host enables the tuning of the chiroptical properties of the emitting layers in electroluminescence devices, although its effects remain marginal. Our synthetic strategy provides particular benefits over previous approaches that rely on phase separation and insulating chiral additives.

Author contributions

J. H. designed and performed most of the experiments, analyzed the data, and wrote the manuscript. S. K. obtained the CPL spectra, and fabricated and tested the devices. G. P. synthesized the Pt dopants. Y. L. and H. K. assisted the CPL measurements and the device experiments. S. K. synthesized GraHIL. T.-W. L. supervised the work at Seoul National University. C. K. and Y. Y. coordinated all of the experiments and analyses, and co-wrote the manuscript. All authors contributed to discussion on the study, and edited the manuscript.

Conflicts of interest

There are no conflicts to declare.

Acknowledgements

Notes and references

1 M. Schadt, Annu. Rev. Mater. Sci., 1997, 27, 305–379.
2 T. Kim, S. Kim, M.-J. Gim and S.-W. Choi, J. Korean Phys. Soc., 2013, 62, 713–717.
3 G. Muller, Dalton Trans., 2009, 9692–9707.
4 J. Yuasa, T. Ohno, H. Tsumatori, R. Shiba, H. Kamikubo, M. Kataoka, Y. Hasegawa and T. Kawai, Chem. Commun., 2013, 49, 4604–4606.
5 H. Koike, K. Nozaki and M. Iwamura, Chem.–Asian J., 2020, 15, 85–90.
6 C. P. Montgomery, B. S. Murray, E. J. New, R. Pal and D. Parker, Acc. Chem. Res., 2009, 42, 925–937.
7 R. Naaman and D. H. Waldeck, J. Phys. Chem. Lett., 2012, 3, 2178–2187.
8 R. Naaman, Y. Paltiel and D. H. Waldeck, Nat. Rev. Chem., 2019, 3, 250–260.
9 R. Carr, N. H. Evans and D. Parker, Chem. Soc. Rev., 2012, 41, 7673–7686.
10 S. Furumi, Chem. Rec., 2010, 10, 394–408.
11 F. Song, G. Wei, X. Jiang, F. Li, C. Zhu and Y. Cheng, Chem. Commun., 2013, 49, 5772–5774.
12 M. Seitz, E. G. Moore, A. J. Ingram, G. Muller and K. N. Raymond, J. Am. Chem. Soc., 2007, 129, 15468–15470.

13 C. Wagenknecht, C.-M. Li, A. Reingruber, X.-H. Bao, A. Goebel, Y.-A. Chen, Q. Zhang, K. Chen and J.-W. Pan, *Nat. Photonics*, 2010, **4**, 549–552.

14 J. F. Sherson, H. Krauter, R. K. Olsson, B. Julsgaard, K. Hammerer, I. Cirac and E. S. Polzik, *Nature*, 2006, **443**, 557–560.

15 H. Li, H. Li, W. Wang, Y. Tao, S. Wang, Q. Yang, Y. Jiang, C. Zheng, W. Huang and R. Chen, *Angew. Chem., Int. Ed.*, 2020, **59**, 4756–4762.

16 R. J. Cave, *Science*, 2009, **323**, 1435–1436.

17 X.-F. Luo, H.-B. Han, Z.-P. Yan, Z.-G. Wu, J. Su, J.-W. Zou, Z.-Q. Zhu, Y.-X. Zheng and J.-L. Zuo, *ACS Appl. Mater. Interfaces*, 2020, **12**, 23172–23180.

18 Y. Wang, Y. Zhang, W. Hu, Y. Quan, Y. Li and Y. Cheng, *ACS Appl. Mater. Interfaces*, 2019, **11**, 26165–26173.

19 F. Song, Z. Xu, Q. Zhang, Z. Zhao, H. Zhang, W. Zhao, Z. Qiu, C. Qi, H. Zhang, H. H. Y. Sung, I. D. Williams, J. W. Y. Lam, Z. Zhao, A. Qin, D. Ma and B. Z. Tang, *Adv. Funct. Mater.*, 2018, **28**, 1800051.

20 F. Zinna, M. Pasini, F. Galeotti, C. Botta, L. Di Bari and U. Giovanella, *Adv. Funct. Mater.*, 2017, **27**, 1603719.

21 F. Zinna, U. Giovanella and L. Di Bari, *Adv. Mater.*, 2015, **27**, 1791–1795.

22 M. Oda, H.-G. Nothofer, G. Lieser, U. Scherf, S. C. J. Meskers and D. Neher, *Adv. Mater.*, 2000, **12**, 362–365.

23 Z. -G. Wu, H. -B. Han, Z. -P. Yan, X. -F. Luo, Y. Wang, Y. -X. Zheng, J. -L. Zuo and Y. Pan, *Adv. Mater.*, 2019, **31**, 1900524.

24 Y. Yang, R. C. da Costa, D.-M. Smilgies, A. J. Campbell and M. J. Fuchter, *Adv. Mater.*, 2013, **25**, 2624–2628.

25 J. Han, S. Guo, J. Wang, L. Wei, Y. Zhuang, S. Liu, Q. Zhao, X. Zhang and W. Huang, *Adv. Opt. Mater.*, 2017, **5**, 1700359.

26 M. Li, S.-H. Li, D. Zhang, M. Cai, L. Duan, M.-K. Fung and C.-F. Chen, *Angew. Chem., Int. Ed.*, 2018, **57**, 2889–2893.

27 M. Li, Y.-F. Wang, D. Zhang, L. Duan and C.-F. Chen, *Angew. Chem., Int. Ed.*, 2020, **59**, 3500–3504.

28 Z.-P. Yan, X.-F. Luo, W.-Q. Liu, Z.-G. Wu, X. Liang, K. Liao, Y. Wang, Y.-X. Zheng, L. Zhou, J.-L. Zuo, Y. Pan and H. Zhang, *Chem.–Eur. J.*, 2019, **25**, 5672–5676.

29 J. R. Brandt, X. Wang, Y. Yang, A. J. Campbell and M. J. Fuchter, *J. Am. Chem. Soc.*, 2016, **138**, 9743–9746.

30 E. Peeters, M. P. T. Christiaans, R. A. J. Janssen, H. F. M. Schoo, H. P. J. M. Dekkers and E. W. Meijer, *J. Am. Chem. Soc.*, 1997, **119**, 9909–9910.

31 Y. Zhang, X. Zhang, H. Zhang, Y. Xiao, Y. Quan, S. Ye and Y. Cheng, *J. Phys. Chem. C*, 2019, **123**, 24746–24753.

32 T.-Y. Li, Y.-M. Jing, X. Liu, Y. Zhao, L. Shi, Z. Tang, Y.-X. Zheng and J.-L. Zuo, *Sci. Rep.*, 2015, **5**, 14912.

33 D.-W. Zhang, M. Li and C.-F. Chen, *Chem. Soc. Rev.*, 2020, **49**, 1331–1343.

34 D.-M. Lee, J.-W. Song, Y.-J. Lee, C.-J. Yu and J.-H. Kim, *Adv. Mater.*, 2017, **29**, 1700907.

35 H. Sakai, S. Shinto, J. Kumar, Y. Araki, T. Sakanoue, T. Takenobu, T. Wada, T. Kawai and T. Hasobe, *J. Phys. Chem. C*, 2015, **119**, 13937–13947.

36 L. Wan, J. Wade, X. Shi, S. Xu, M. J. Fuchter and A. J. Campbell, *ACS Appl. Mater. Interfaces*, 2020, **12**, 39471–39478.

37 G. Fu, Y. He, W. Li, B. Wang, X. Lu, H. He and W.-Y. Wong, *J. Mater. Chem. C*, 2019, **7**, 13743–13747.

38 M. Oda, H.-G. Nothofer, U. Scherf, V. Sunjic, D. Richter, W. Regenstein and D. Neher, *Macromolecules*, 2002, **35**, 6792–6798.

39 X. H. Yang, D. Neher, C. Spitz, E. Zojer, J. L. Bredas, R. Guntner and U. Scherf, *J. Chem. Phys.*, 2003, **119**, 6832–6839.

40 M. R. Craig, P. Jonkheijm, S. C. J. Meskers, A. P. H. J. Schenning and E. W. Meijer, *Adv. Mater.*, 2003, **15**, 1435–1438.

41 J. Gilot, R. Abbel, G. Lakhwani, E. W. Meijer, A. P. H. J. Schenning and S. C. J. Meskers, *Adv. Mater.*, 2010, **22**, E131–E134.

42 G. Lakhwani and S. C. J. Meskers, *J. Phys. Chem. Lett.*, 2011, **2**, 1497–1501.

43 G. Lakhwani and S. C. J. Meskers, *J. Phys. Chem. A*, 2012, **116**, 1121–1128.

44 K. Watanabe, Y. Koyama, N. Suzuki, M. Fujiki and T. Nakano, *Polym. Chem.*, 2014, **5**, 712–717.

45 S. T. Duong and M. Fujiki, *Polym. Chem.*, 2017, **8**, 4673–4679.

46 J. Li, X. Peng, C. Huang, Q. Qi, W.-Y. Lai and W. Huang, *Polym. Chem.*, 2018, **9**, 5278–5285.

47 A. Satrijo, S. C. J. Meskers and T. M. Swager, *J. Am. Chem. Soc.*, 2006, **128**, 9030–9031.

48 J. N. Wilson, W. Steffen, T. G. McKenzie, G. Lieser, M. Oda, D. Neher and U. H. F. Bunz, *J. Am. Chem. Soc.*, 2002, **124**, 6830–6831.

49 S. Fukao and M. Fujiki, *Macromolecules*, 2009, **42**, 8062–8067.

50 Y. Nakano, F. Ichiyanagi, M. Naito, Y. Yang and M. Fujiki, *Chem. Commun.*, 2012, **48**, 6636–6638.

51 K. Watanabe, I. Osaka, S. Yorozuya and K. Akagi, *Chem. Mater.*, 2012, **24**, 1011–1024.

52 B. M. W. Langeveld-Voss, R. A. J. Janssen, M. P. T. Christiaans, S. C. J. Meskers, H. P. J. M. Dekkers and E. W. Meijer, *J. Am. Chem. Soc.*, 1996, **118**, 4908–4909.

53 K. Watanabe, T. Sakamoto, M. Taguchi, M. Fujiki and T. Nakano, *Chem. Commun.*, 2011, **47**, 10996–10998.

54 D. Di Nuzzo, C. Kulkarni, B. Zhao, E. Smolinsky, F. Tassinari, S. C. J. Meskers, R. Naaman, E. W. Meijer and R. H. Friend, *ACS Nano*, 2017, **11**, 12713–12722.

55 K. Meerholz, B. L. Volodin, Sandalphon, B. Kippelen and N. Peyghambarian, *Nature*, 1994, **371**, 497–500.

56 Y. Kawamura, S. Yanagida and S. R. Forrest, *J. Appl. Phys.*, 2002, **92**, 87–93.

57 E. Chiellini, R. Solaro, O. Colella and A. Ledwith, *Eur. Polym. J.*, 1978, **14**, 489–496.

58 V. Percec, M. Obata, J. G. Rudick, B. B. De, M. Glodde, T. K. Bera, S. N. Magonov, V. S. K. Balagurusamy and P. A. Heiney, *J. Polym. Sci., Part A: Polym. Chem.*, 2002, **40**, 3509–3533.

59 Z.-B. Zhang, M. Motonaga, M. Fujiki and C. E. McKenna, *Macromolecules*, 2003, **36**, 6956–6958.

60 L. Angiolini, T. Benelli, L. Giorgini, F. Mauriello and E. Salatelli, *Macromol. Chem. Phys.*, 2006, **207**, 1805–1813.

61 H. Zhao, F. Sanda and T. Masuda, *J. Polym. Sci., Part A: Polym. Chem.*, 2007, **45**, 253–261.

62 J. Qu, R. Kawasaki, M. Shiotsuki, F. Sanda and T. Masuda, *Polymer*, 2007, **48**, 467–476.

63 J. Qu, M. Shiotsuki, F. Sanda and T. Masuda, *Macromol. Chem. Phys.*, 2007, **208**, 823–832.

64 J. Qu, Y. Suzuki, M. Shiotsuki, F. Sanda and T. Masuda, *Polymer*, 2007, **48**, 4628–4636.

65 F. Sanda, R. Kawasaki, M. Shiotsuki and T. Masuda, *J. Polym. Sci., Part A: Polym. Chem.*, 2007, **45**, 4450–4458.

66 F. Sanda, R. Kawasaki, M. Shiotsuki, T. Takashima, A. Fujii, M. Ozaki and T. Masuda, *Macromol. Chem. Phys.*, 2007, **208**, 765–771.

67 L. Angiolini, T. Benelli, L. Giorgini, A. Golemme, F. Mauriello, E. Salatelli and R. Termine, *Macromol. Chem. Phys.*, 2008, **209**, 944–956.

68 Y. Hu, F. Song, Z. Xu, Y. Tu, H. Zhang, Q. Cheng, J. W. Y. Lam, D. Ma and B. Z. Tang, *ACS Appl. Polym. Mater.*, 2019, **1**, 221–229.

69 X. Ma, E. Abdel Azeem, X. Liu, Y. Cheng and C. Zhu, *J. Mater. Chem. C*, 2014, **2**, 1076–1084.

70 M. Belletête, M. Bedard, M. Leclerc and G. Durocher, *J. Mol. Struct.*, 2004, **679**, 9–15.

71 G. E. Johnson, *J. Chem. Phys.*, 1975, **62**, 4697–4709.

72 Y. K. Moon, J.-S. Huh, S. Kim, S. Kim, S. Y. Yi, J.-J. Kim and Y. You, *ACS Appl. Polym. Mater.*, 2020, **2**, 604–617.

73 Y.-C. Wei, Z. Zhang, Y.-A. Chen, C.-H. Wu, Z.-Y. Liu, S.-Y. Ho, J.-C. Liu, J.-A. Lin and P.-T. Chou, *Commun. Chem.*, 2019, **2**, 10.

74 A. J. Musser, S. K. Rajendran, K. Georgiou, L. Gai, R. T. Grant, Z. Shen, M. Cavazzini, A. Ruseckas, G. A. Turnbull, I. D. W. Samuel, J. Clark and D. G. Lidzey, *J. Mater. Chem. C*, 2017, **5**, 8380–8389.

75 A. Wrona-Piotrowicz, J. Zakrzewski, R. Métivier, A. Brosseau, A. Makal and K. Woźniak, *RSC Adv.*, 2014, **4**, 56003–56012.

76 T. Kayano, S. Takayasu, K. Sato and K. Shinozaki, *Chem.–Eur. J.*, 2014, **20**, 16583–16589.

77 B. Ma, P. I. Djurovich and M. E. Thompson, *Coord. Chem. Rev.*, 2005, **249**, 1501–1510.

78 G. F. Johnson and D. J. Graves, *Biochemistry*, 1966, **5**, 2906–2911.

79 M. Wakabayashi, S. Yokojima, T. Fukaminato, K.-i. Shiino, M. Irie and S. Nakamura, *J. Phys. Chem. A*, 2014, **118**, 5046–5057.

80 N. Harada, S.-M. L. Chen and K. Nakanishi, *J. Am. Chem. Soc.*, 1975, **97**, 5345–5352.

81 N. Harada and K. Nakanishi, *J. Am. Chem. Soc.*, 1968, **90**, 7351–7352.

82 M. M. Green, M. P. Reidy, R. D. Johnson, G. Darling, D. J. O'Leary and G. Willson, *J. Am. Chem. Soc.*, 1989, **111**, 6452–6454.

83 T. Ikai, S. Shimizu, S. Awata and K.-i. Shinohara, *Macromolecules*, 2018, **51**, 2328–2334.

84 J. V. Selinger and R. L. B. Selinger, *Phys. Rev. E: Stat., Nonlinear, Soft Matter Phys.*, 1997, **55**, 1728–1731.

85 M. M. Green, J. -W. Park, T. Sato, A. Teramoto, S. Lifson, R. L. B. Selinger and J. V. Selinger, *Angew. Chem., Int. Ed.*, 1999, **38**, 3138–3154.

86 V. Jain, K.-S. Cheon, K. Tang, S. Jha and M. M. Green, *Isr. J. Chem.*, 2011, **51**, 1067–1074.

87 S. K. Jha, K.-S. Cheon, M. M. Green and J. V. Selinger, *J. Am. Chem. Soc.*, 1999, **121**, 1665–1673.

88 G. Heinrich, S. Schoof and H. Gusten, *J. Photochem.*, 1974, **3**, 315–320.

89 T. -H. Han, M. R. Choi, S. -H. Woo, S. -Y. Min, C. -L. Lee and T. -W. Lee, *Adv. Mater.*, 2012, **24**, 1487–1493.

90 T. D. Anthopoulos, J. P. J. Markham, E. B. Namdas, I. D. W. Samuel, S.-C. Lo and P. L. Burn, *Appl. Phys. Lett.*, 2003, **82**, 4824–4826.

91 R. Arunchai, T. Sudyoadsuk, N. Prachumrak, S. Namuangruk, V. Promarak, M. Sukwattanasinitt and P. Rashatasakhon, *New J. Chem.*, 2015, **39**, 2807–2814.